FULL RESEARCH ARTICLE

Influence of post-heat treatment on microstructure, texture, and mechanical properties of 18Ni-300 maraging steel fabricated by using LPBF technique

Satish Prakash Karlapudy[1] · T. Nancharaiah[2] · V. V. Subba Rao[1]

Abstract

The research paper focuses on the mechanical properties of post-heat treatments as a function of build orientation and laser scan strategy, i.e., direct aging (DAT-490 °C/4 h) and solutionizing + dual subsequent aging (SAAT-940 °C/2 h + 490 °C/1 h + 490 °C/3 h) heat treatments are applied to maraging steel produced by laser powder bed fusion (LPBF). The experimental works have been carried out using the Taguchi L_9 Orthogonal array approach. There were three different scanning patterns (SS-X, SS-XY, and SS-XR) and build orientations (YX, XZ, and ZX) were used. Using the scan strategy SS-XY, properties are generally superior in a horizontal orientation due to thermal history variations. As compared to all other orientations, vertical components had lower mechanical performance values in terms of strength. With different scan strategies, each sample has a different microstructure consisting of tiny pores and cracks on top surface for various post-heat treatments. X-ray diffraction showed peaks of austenite and ferrite with the highest intensity. The results indicate that LPBF heat treatments change the microstructure, crystallographic texture, and phase transformations of maraging steel produced with LPBF, affecting its hardness and ultimate strength.

Keywords Post-heat treatment · Microstructure · Build orientation · Scan strategies · Maraging steel · LPBF

1 Introduction

Additive manufacturing techniques like laser powder bed fusion (LPBF) have gained a lot of attention recently [1]. This is because LPBF has much potential to become a helpful tool. The LPBF method is beneficial, because it permits the layer-by-layer manufacturing of superior metallic materials with complicated patterns from the raw powders in precision geometric parts [2] that cannot be accomplished with the use of conventional manufacturing processes. LPBF-made components that do not undergo heat treatments often display qualities equivalent to or superior to those of conventionally manufactured components. This is because quick solidification and cooling are intrinsic behaviors that occur during LPBF manufacturing. After several years of rapid development, various high-performance metal parts can be manufactured using LPBF. There are several types of alloys used in these systems, including Ti-alloys [3, 4], Fe-alloys [5, 6], and Ni-based superalloys [7]. Therefore, in recent years, LPBF has become highly attractive for fabricating this high-performance alloy. Most previous studies on LPBF Manufactured maraging steels have concentrated on the optimization of the process, the characterization of the material's microstructure, and the performance characteristics. Maraging steel is an ultra-high-resistance, excellent toughness, high-hardness, weldability, and extensively used in aerospace, automotive casting areas [8] and space technologies [9] to characterize the surface conditions of LPBF-fabricated parts that can be repaired including turbine blades and integrated blade rotors [10]

According to previous studies, AM maraging steels with full density are as efficient as conventionally manufactured steels [11–13]. In addition, the aging heat treatment of intermetallic compounds that have undergone precipitation hardening may result in improved mechanical qualities [14]. These studies have primarily focused on optimizing process parameters or mechanical properties after aging to prove this material is

✉ Satish Prakash Karlapudy
satishkarlapudy@gmail.com

[1] Department of Mechanical Engineering, Jawaharlal Nehru Technological University, Kakinada, India

[2] Department of Mechanical Engineering, Bapatla Engineering College, Bapatla, India

suitable for LPBF. Using a statistical optimization method, for instance, Casalino et al. [11] investigated the effect of various process parameters on the relative density of LPBF maraging steel. Bai et al. [15] investigated how varying the laser intensity and scanning speed affected vaporization and spatter for an orthogonal study for processing of maraging steel. Kempen et al. [13] examined LPBF maraging steel through several aging treatments. It was seen that as-built samples had significantly lower ductility and a significant increase in strength after aging. The samples exhibited 58 HRC hardness and 2217 MPa UTS after 5 h of aging at 480 °C.

The literature review above suggests that optimal process parameters enable LPBF to produce maraging steel components with nearly full density. The LPBF maraging steel often undergoes post-heat treatments to improve mechanical performance. Traditional heat treatments can be divided into three types: solution, direct aging, and solution + aging treatment [16, 17]. The ultimate strength and elongation of vertical-built samples were lower than that of horizontal-built samples for anisotropic behavior observed by Mutua et al. [18]. The mechanical characteristics of the LPBF-printed parts were analyzed by Song et al. [17]. They found that, in contrast to aged materials, materials subjected to solution-aging conditions were weaker and more ductile. In addition, Tan et al. [19] suggested that LPBF-built maraging steel is best treated with a combined solution-aging treatment. Subsequent aging formed by Ni-rich Martensite and stated that during the first stage of aging of maraging steel and other grades, Nickel-based precipitates (primarily Ni_3Ti, Ni_3Mo) form. In contrast, Fe-based precipitates (Fe_2Mo and Fe_7Mo_6) substitute the previously developed species in the second stage. Aging promotes austenite reversion by releasing nickel from Ni_3Ti and Ni_3Mo precipitates. Due to a high austenite content, aging may promote softening and fracture softening [20–24]. Furthermore, heat treatment can improve the mechanical characteristics of intermetallic compounds through precipitation and hardening [14]. According to Kempen et al. [13], LPBF maraging steels can achieve good tensile properties without solutionizing. The martensite phase was higher than 96% in the as-built and aged maraging steel samples, and elongation until fracture decreased from 13 to 2%. Most of the research has been done so far to assess the LPBF printability of various engineering materials, and most of the investigations are still ongoing.

Extensive literature on different build orientations with heat treatments for AM of various materials is available. According to Oliveira et al. [25], building orientation and post-heat treatment conditions affect the maraging steel defect formation process and tensile properties. The material's performance was enhanced due to the aging treatment, which reduced the probability of deformity coalescence. According to Vishwakarma et al. [26], the heat treatment improved the strength of the samples without decreasing their ductility microvoid coalescence-induced work softening and

reversion with dimples in all samples. A possible reason for this finding is that the post-treatment improved the tensile characteristics of martensite to austenite. Mutua et al. [18] observed that LPBF-fabricated maraging steel comprised mostly during direct aging without solutionizing treatment will increase austenite because of martensite to austenite conversion. Meneghetti et al. [27] evaluated tensile and fatigue factors of maraging steel in various build orientations, i.e., 0° and 90°. In both their as-built and aged forms, tensile testing found that the mechanical properties of samples made at 0° and 90° were similar. According to Bai et al. [15], LPBF-treated steel exhibited lower ductility and hardness than wrought steel. Reduced ductility was observed after heat treatment.

Recent research focused on the scan strategies of various AM materials available. In their study, Geiger et al. [28] discovered that the texture LPBF Inconel 738LC was dependent on how the temperature gradient was oriented in the build-up axis and that this orientation can alter the direction of < 001 > crystals based on the findings of their research into the effect of various laser scanning techniques. They disclosed the availability of a conversion method for triple-layered stacks to transverse isotropy. Gu et al. [29] examined the impact of scan and component arrangement on LPBF 316L stainless steel performance. Crystallographic alterations affect mechanical properties by modifying the texture-grain growth orientation correlation. As a result of using a double zig-zag melt with a 90° rotation, the texture in the perpendicular direction is very strong, resulting in excellent ductility, and strength. Almangour et al. [30] demonstrated that both double-pass and cross-directional scanning significantly increased density. Furthermore, the change in TiC composition and grain orientation caused anisotropy due to localized heat flux. Condruz et al. [31] in both XZ- and YZ-planes, long columnar grains developed during multiple laser passes during a 90° scanning strategy, resulting from partial remelting. In contrast, equiaxed grains were produced in the XY-plane scanning at 67°, although at a lesser magnitude, resulting in the formation of long columnar grains on the specimens. Liu et al. [32] compared with the SS-XY45, the SS-X had a larger YS. A modified grain structure results in improved ductility, as intergranular brittle fracture mode changes to transgranular ductile fracture mode resulting in refined grains with higher yield strength.

The above literature reviewed that the ductility of maraging steel decreases substantially as the strength of the steel increases after heat treatment. There have been very few studies that examine how ductility can be enhanced by heat treatments for AM maraging steel. There are also only a few investigations that take into account the effects of factors such as build orientation and scan strategies in addition to a comprehensive analysis of microstructural effects obtained by scanning electron microscopy, electron back-scattered diffraction

Table 1 EOS 2020 maraging steel powder chemical composition (wt%) [55]

Element	Ni	Mo	Co	Ti	Al	Cr	C	Mn	P,S	Fe
MS-1 [55]	17–19	4.5–5.2	8.5–9.5	0.6–0.80	0.05–0.15	0–0.5	0–0.03	0–0.1	0–0.01	BAl
EDX	18.17	4.8	9.41	0.8	0.12	0.16	0	0.02	0	66.52
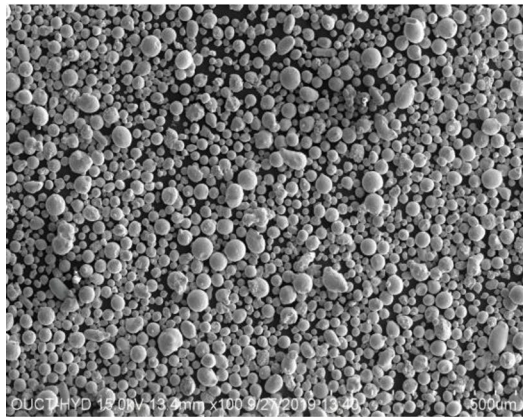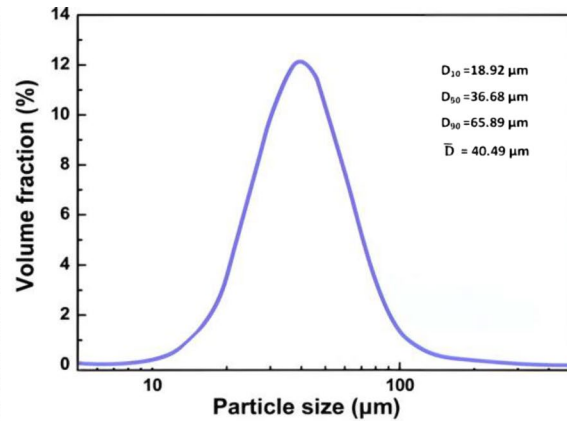
(a)   (b)

Fig. 1 SEM microstructure of **a** 18Ni-300 Maraging steel powder and **b** particle-size distribution

that affects the mechanical characteristics of specimens, which are extremely rare because the mechanical properties of additively manufactured steels (AM steels) differ significantly from those of conventional steels. However, the influence of build orientation and scan techniques on mechanical qualities has yet to be adequately investigated in combination with post-treatment. This study evaluates three distinct LPBF scanning procedures with various heat treatments on Maraging steel. The effects of direct aging treatment (DAT) and solution + aging + aging (SAAT) on 18Ni-300 maraging steel were investigated after two different heat treatments of anisotropy.

2 Experimental details

Maraging steel (MS1) powder was utilized as a raw material in this study. It was supplied by EOS GmbH (Germany). Through a process of atomization, the powder produces a gas that is subsequently released into the air. A mild steel substrate with powder particles between 40 and 50 µm in size was used for the test. Table 1 displays the powder's chemical composition, Fig. 1 depicts the powder's microstructure and particle-size distribution, and Fig. 2 shows the EDS results for an as-built sample.

Analysis of an EDS elemental map (Fig. 3) shows that Fe, Mo, Ni, and Co are evenly distributed, supporting homogenous deposition throughout the LPBF process.

Before conducting LPBF, the plate was preheated to 40 °C using an integrated heater. Continuous nitrogen
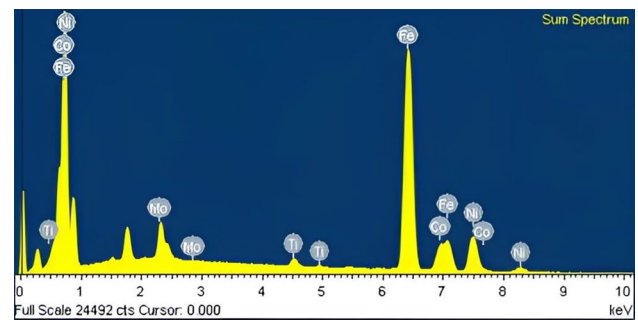
Fig. 2 EDS for as-printed sample

pumping kept the oxygen concentration in the process vacuum chamber at 1.6%. At the LPBF machine, a $35 \times 5 \times 1.7$ mm³ specimen was produced using parameters of 285W laser power, 40 µm layer thickness, 960 mm/s scanning speed, and 110 µm hatch distance. The primary laser process parameters are shown in Table 2. The following criteria were used based on a review of the relevant literature [15, 33]: using a 40 µm layer thickness, 250–370 W laser power, 50–150 µm hatch spacing, 500–1500 mm/s scanning speed, and 67.47 J/mm³ energy density. Three different laser scanning techniques were used in this study (bi-directional, zig-zag with 67° rotation, and cross-directional). The zig-zag is the most common X-axis method for tensile plates, which is performed at an angle of 90° to the load axis. The second strategy included X- and Y-axis scans that were zig-zagged and crossed at right angles to one another and a 67° zig-zag

**Fig. 3** EDS mapping image of the 18 Ni-300 Maraging steel of **a** Fe, **b** Mo, **c** Ni, and **d** Co
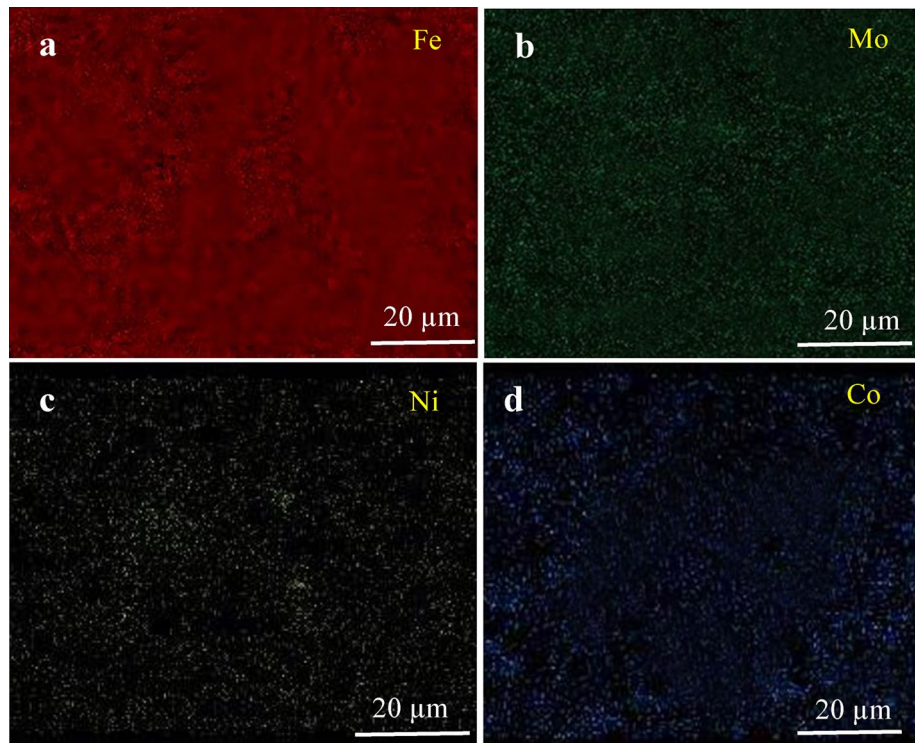
Table 2 Number of experiments at various process parameters

Exp	Build orientation	Scan strategy (SS)
1	YX	SS-X
2	YX	SS-XY
3	YX	SS-XR
4	XZ	SS-X
5	XZ	SS-XY
6	XZ	SS-XR
7	ZX	SS-X
8	ZX	SS-XY
9	ZX	SS-XR

laser scan as displayed in Fig. 4a–c. Several building orientations and tensile test specimens are shown in Fig. 5. The specimens intended for machining tensile test pieces were manufactured on three different building orientations: along *X*-, *Y*-, *Z*-axis. The naming convention uses two letters. The first letter is the axis of the machine in which the longest axis of the sample lies. The second letter is the machine axis in which the second longest sample axis lies. Here YX, XZ and ZX are the flat horizontal specimen build orientation, edge horizontal specimen build orientation, and vertical specimen build orientation. Here 'X', 'Y', and 'Z' are the lengths in X, Y, Z build-directions. The three different experimental

Fig. 4 Three different scanning strategies, namely **a** SS-X, **b** SS-XY, and **c** SS-XR
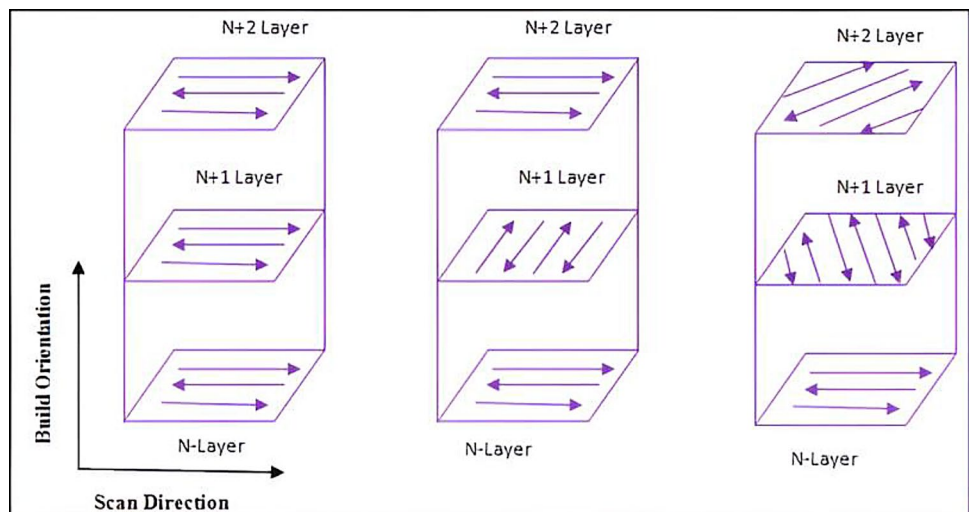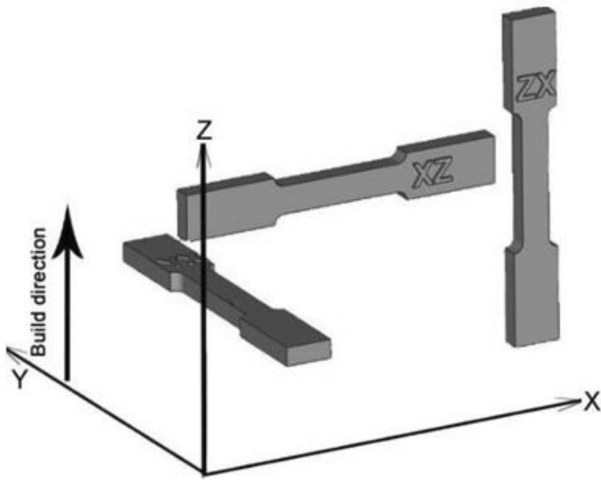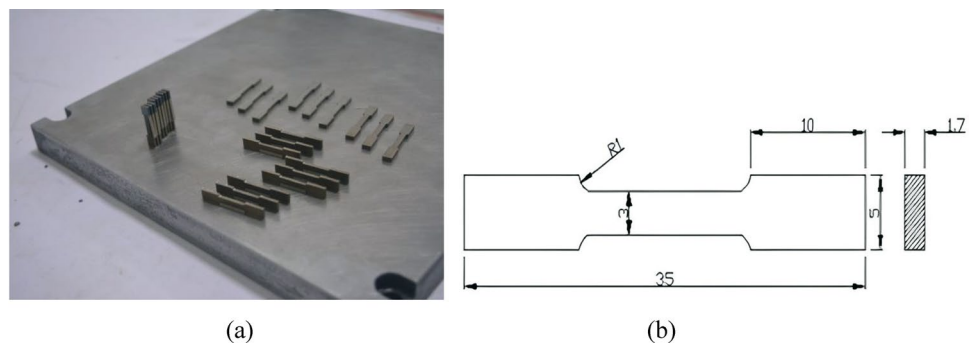
Fig. 5 Building directions for tensile testing parts

setups are shown in Table 2. To examine the microstructure and mechanical properties of the samples, they are wire-EDM sliced (Model-Agie Cut Progress Wed-003).

Experiments were conducted to compare the mechanical properties of as-built (AB), direct aging treatment (DAT), and solution + aging + aging treatments (SAAT) setups with respect to the orientation of the build. Microhardness was measured on five different locations for each sintered part and then averaged using a Rockwell hardness tester (MVD402) with a 0.2 kgf force. A sub-size tensile sample is built with dimensions of 35 mm (length), 5 mm (width), and 1.7 mm (thickness), as illustrated in Fig. 6a, b. Three samples' mean mechanical characteristics were evaluated using a 1 mm/min crosshead speed on an ASTM E8-based universal testing equipment. The average roughness R_z of a printed sample is assessed using a portable Mitutoyo Surf Tester SJ.201, an XRD facility equipped with a Shimadzu-7000 2KW diffractometer with a step scale of 0.02 used to identify the phase composition of manufactured components in the 2θ range of 30°–90°. Lattice spacing (λ) and $\sin^2\psi$ were used for the measurements at a Bragg's angle (2θ) of 156°[34] and BCC [211].

"The fracture surface morphology was examined by using a scanning electron microscope (SEM) (make- S-3700N Hitachi), and a particle-size distribution analyzer (make-Horiba-SZ100) was used to investigate the particle-size distribution. The specimen's microstructural characteristics were studied using a scanning electron microscope. Electron dispersion spectroscopy (EDX) analysis was performed by Fei Quanta 200 HV SEM with a TSL device. Using a Fei Quanta 3D FEG model, Electron back-scattered diffraction (EBSD) mapping was performed on the top surfaces with a 0.3 μm step size" [35]. TSL-OIM was used for the analysis of the pictures. The post-heat treatments (ERF) used an electrical resistance heating furnace. Heat-treatment foil was used to protect samples from oxidation throughout the process. Maraging steel is subjected to direct aging (DAT-490 °C/4 h) and solution heat treatment + dual subsequent aging (SAAT-940 °C/2 h + 490 °C/1 h + 490 °C/3 h) heat treatments manufactured by LPBF and heat treatment conditions are given in Table 3
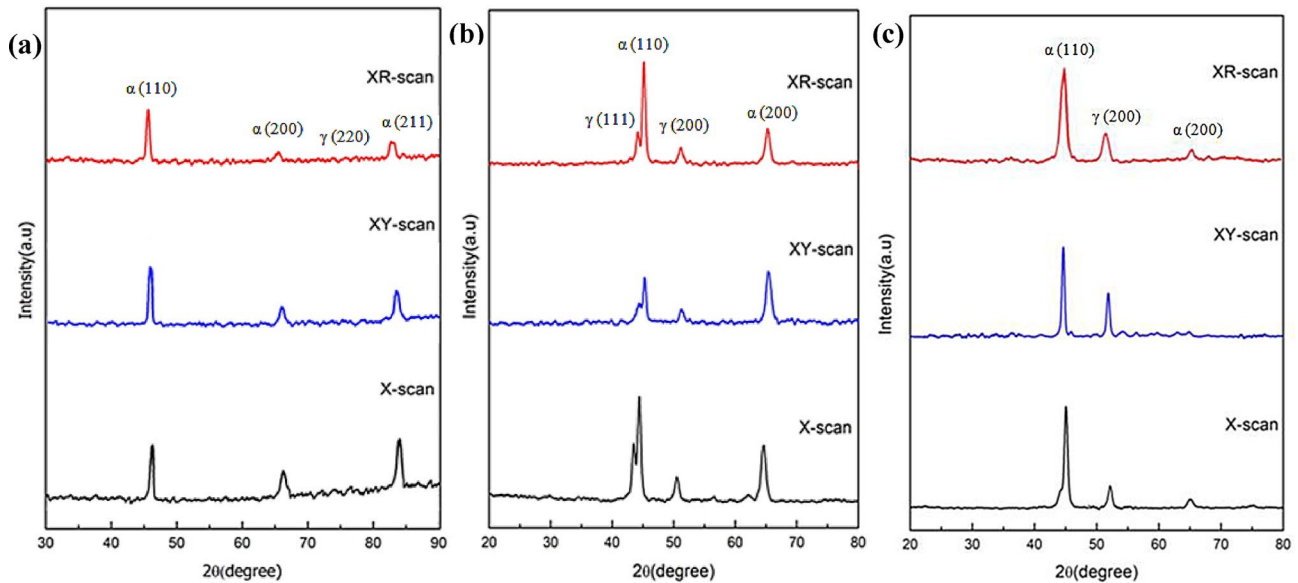
3 Results and discussion

3.1 XRD analysis

The as-fabricated and post-heated-treated XRD patterns for X, XY, and XR Laser Scanning Strategies of LPBF specimens are displayed in Fig. 7. Table 4 summarizes the volumetric percentages of martensite (α) and austenite (γ) phases of LPBF specimens using Rietveld refinement analysis and used to calculate the phases. Compared to the as-fabricated

Table 3 Heat-treatment conditions

Phase	Heat-treatment process
As built (AB)	No treatment
Direct aged treatment (DAT)	490 °C/4 h + air cooling
(Solution + aged) + aged (SAAT)	(940 °C/2 h + air cooling) + (490 °C/1 h + air cooling) + 490 °C/3 h + air cooling

Fig. 6 **a** Printed parts build on mild steel substrate, and **b** ASTEM8 tensile piece

(a)

(b)

Fig. 7 XRD patterns of X, XY, and XR laser scanning strategies for **a** AB, **b** DAT, and **c** SAAT conditions

Table 4 Values obtained by Rietveld refinement analysis

Specimen condition	Scan strategy	Austenite (γ)	Martensite (α)
As-built	SS-X	5.40%	93.60%
	SS-XY	9.20%	90.80%
	SS- XR	5.80%	94.20%
Aging	SS- X	8.80%	91.2%
	SS-XY	10.7%	89.30%
	SS-XR	7.50%	92.50%
Solu-tion+aging+aging	SS-X	6.00%	94.00%
	SS-XY	6.50%	93.50%
	SS-XR	3.62%	96.38%

specimen, the amount of γ phase in the age-treated sample was more significant than that in the as-fabricated sample. Only a few volume fractions of austenite γ (111) remain after SAAT and integrated solution and dual-age treatments.

According to Prakash et al. [36], With XR and X scans, the formation of γ-austenite remains at approximately 38% and 34%, respectively, compared to XY scans was due to the change in the heat flow path in the XY scan process results in a different heat flow path as seen in Fig. 7a. This comparison was carried about by the XY scan technique, which results in a higher solidifying rate by the previous and succeeding layers of the melt pool [19].

The as-built specimen shows a minor peak in the austenite (γ) phase at (220). For aging at 490 °C for 6 h, the (220) peak becomes stronger, suggesting the processing of additional γ phase for the three scan techniques X, XY, and XR, as shown in Fig. 7b. This indicates that the phase change from α to γ occurs during aging. The most evident

attribute suggests that the strength of the γ(200) phase peak has increased. This reveals that the BCC changes to an FCC during direct aging and that high temperatures cause austenite phase growth to occur in other directions. The XRD patterns of X, XY, and XR Laser Scanning Strategies of LPBF SAAT specimens are shown in Fig. 7c. Using the X, XY, and XR scan approaches, to generate a complete martensite matrix using the X, XY, and XR scan method, the SAAT condition induces a phase transfer from γ to α phase, as shown in Fig. 7c. The martensitic phase predominantly rises in the direction of γ (211). Because there are no phase peaks in the SAAT samples, it was concluded that aging would not change the phase after solution treatment [15, 33]. When the as-built specimen was treated to SAAT, the γ (220) peak vanished, suggesting that the phase generated during SAAT was entirely changed into the γ phase during cooling. The initial powder martensite phase changes to austenite due to phase transitions throughout the LPBF process. Separation and unequal distribution of alloying elements during cooling may facilitate martensite transformation to austenite. Previous studies have used a method quite similar to this on [13, 37]

3.2 Phase transformation

A large number of martensite (α) phases and a minor number of austenite (γ) phases were identified in the as-printed part. The volume of phase in the aged sample was higher than that of the as-printed part. During solution treatment, no full martensite phase is generated, Following solution and dual aging treatments, the austenite phase γ (111) reappears in very minor volumes. Although a significant amount of the α phase

was generated in the as-built microstructure, the amount of the γ phase was much smaller. The as-built samples that are subjected to an aging heat treatment result in the formation of $\alpha + \gamma + \gamma^1$ precipitate phases. After subjecting the as-built samples to the SAAT heat treatment, $\alpha + \gamma^1$ and precipitate phases are generated. The material produced in these samples exhibited martensite as the predominate phase (SAAT).

It is possible to generate supersaturated homogeneous α-Fe solid solutions by treating them with a solution in the austenitizing zone. As a result, solution treatment is used to make maximum use of the alloying components while also providing a martensitic matrix that is entirely homogeneous after cooling. The higher austenite percentage after dual aging treatment has been associated with the unavoidable conversion of martensite toward the more stable reversed (γ^1) phase, which occurs during the aging treatment [14, 38].

Our study has a restricted aging duration (4 h), which results in a limited number of precipitates. The primary precipitates found are η-Ni_3Ti, η-Ni_3Al, and η-Ni_3Mo phases, with no evidence of a Fe_2Mo phase. As a result, it is reasonable to summarize the phase transitions that occur during heat treatment as follows.

$$\alpha + \gamma \xrightarrow{\text{490°C aging}} \alpha + \gamma + \gamma' + Ni_3\,(Ti,\,Al,\,Mo)\text{ precipitates}$$

$$\alpha + \gamma \xrightarrow{\text{940°C solution}} \alpha \xrightarrow{\text{490 °C aging}} \gamma \xrightarrow{\text{490 °C aging}} \alpha + \gamma + \gamma' + Ni_3\,(Ti,\,Al,\,Mo)\text{ precipitates}$$
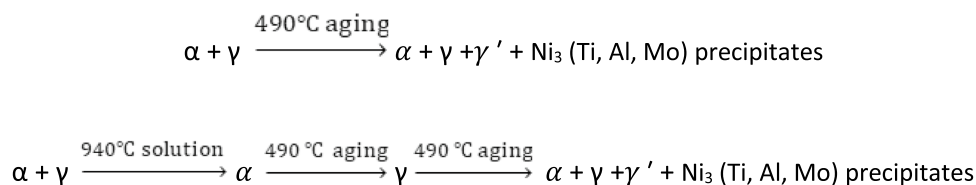
3.3 EBSD mapping and texture analysis

The crystallographic texture characterization of the maraging steels generated by LPBF under various heat treatment modes was carried out utilizing the EBSD patterns and pole figures. Three samples were made using X-scan, XY-scan, and Rot-scan scanning techniques. EBSD investigated their crystallographic texture and crystal orientation maps on the three XY-planes of the three samples for AB, DAT, and SAAT conditions, as shown in Fig. 8a–r. The images mainly reveal grains' shape and size, and distribution in their XY-plane and relative orientation.

The equivalent {110} {100} {111} pole figures derived from the XY-plane of the samples are also shown in Fig. 8j–r. Each layer's X-scan top surface has columnar cells oriented in the building direction for each layer of strong < 111 > texture (violet color) that dominates the X-scan top surface. However, a significant cubic texture < 100 > (red color) was observed, which is followed by the formation of epitaxial development of different textures, as shown in Fig. 8a and

also displayed in Fig. 8j. The top surfaces of the XY scan samples indicates that lack of dominance in any plane, as seen in Fig. 8b and pole Fig. 8k and also, similar observations were found by Bharadwaj et al. [39]. According to Suryawanshi et al. [33], the lack of texture dominance for the XY scan technique is due to heat flux rotation in X- and Y-directions in the following layers. Epitaxial development is also visible on the XY scan technique top surface owing to heat flux rotation in succeeding layers. And in the XR scan strategy, the z-plane orientation map shows intersected lines with 67°, matching the scan direction between adjacent layers with 67°. Crystals are randomly oriented, as illustrated in Fig. 8c and displayed in Fig. 8l.

Epitaxial crystal growth governs the formation of distinct textures in layer-by-layer deposition [40]. In LPBF components, cellular microstructures are always produced along the build direction or transverse to the scan direction. Similar findings were found by Marattukalam et al. [41] using different scan techniques. Deposition of layers results in different textures due to the effect of scan vectors and epitaxial crystal growth [42]. Results showed that cellular micrographs always develop along the build direction in LPBF components. As suggested by Thijs et al. [40], if the heat is carried in the direction of 001 >, the epitaxial grains will develop using an X-scan technique. In this study, epitaxial growth is observed vertically and horizontally along the build direction for the XY-scan strategy. The scanning direction also shows the formation of elongated grains. The same crystallographic orientations as previously solidified grains result in the formation of elongated grains for both scan strategies and also reported similar observations in AlMangour et al. [30]

For the DAT condition, Fig. 8d–f shows that when the scan direction is bi-directional along the build direction, a strong < 110 > texture was found, and there is a weak < 111 > texture along the scan path after direct aging. One of the key findings demonstrates that the columnar cells grew preferentially in the scan direction perpendicular to the < 100 > crystallographic direction. The texture indicates that throughout the LPBF

Fig. 8 Crystal orientation maps **a**–**i** of AB, DAT, and SAAT for different scanning strategies with varying textures and corresponding {111} {110} {100} pole Figures **j**–**r** measured on the top planes
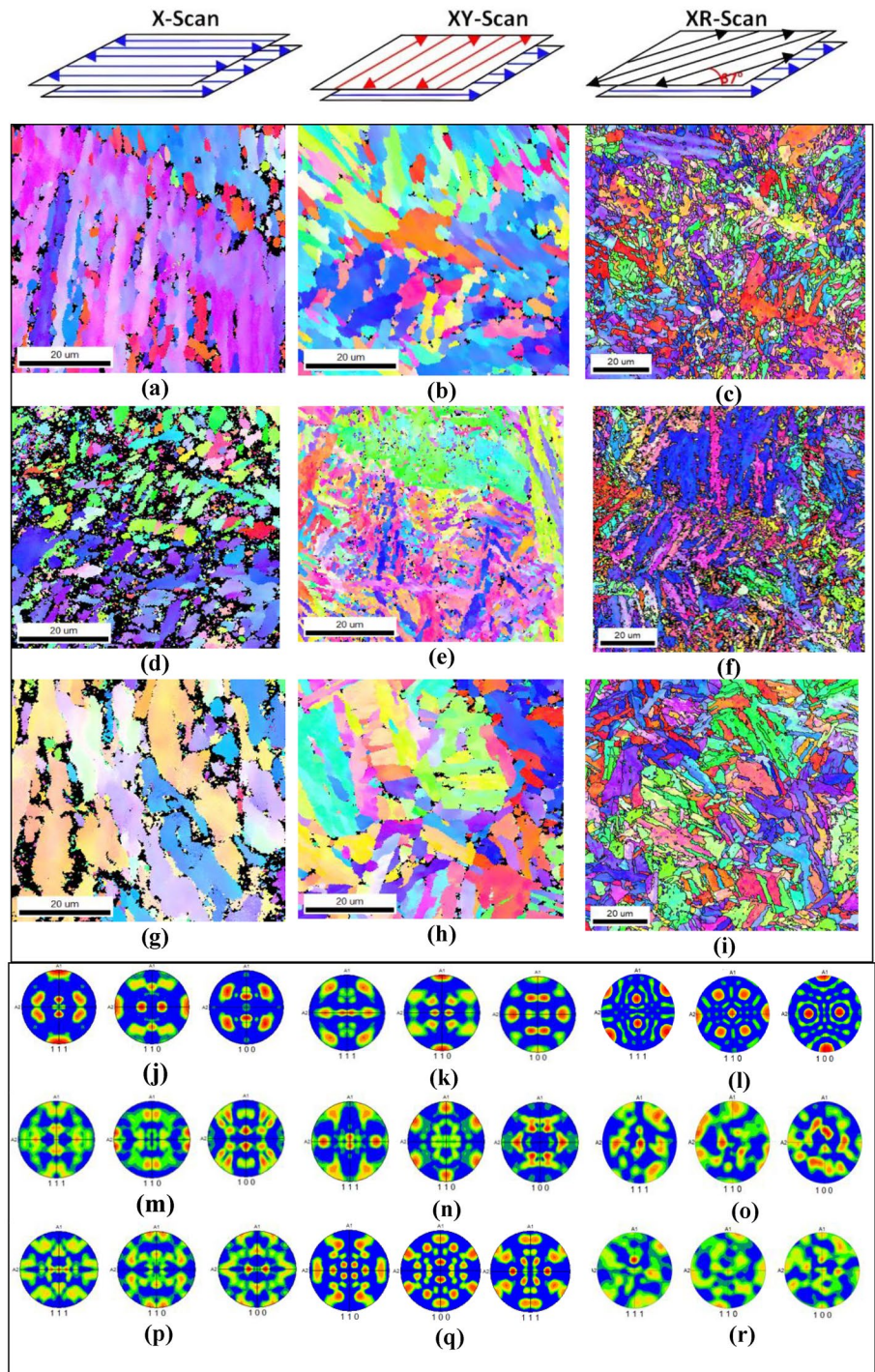
process, < 100 > and < 110 > alignment occurred in three building directions. Most of the crystals of the X and XR samples are randomly oriented, as shown in Fig. 8d, f, and XY samples are textured, as shown in Fig. 8e, and based on the pole Fig. 8m, o, a weak texture in the build direction is observed after aging and similar observation was seen in Podgornic et al. [43]. And the crystals with strong intensity are displayed in Fig. 8n. As a result, it may be concluded that the phase texture was generated during solidification and that crystallographic transitions from γ to α phases occurred as a result of different selections. When just 490 °C aging heat treatment was performed without adding solution treatment (ST), the texture was entirely reproduced, as seen in Fig. 8d–f and it was supported by Tan et al. [44]

When SAAT was performed after aging treatment, many grains were columnar, elongated, and oriented in a similar direction, as seen in Fig. 8p, r. High ductility and tensile strength are achieved in LPBF-built samples because of the scanning method with the rotation angle between successive layers, which disrupts the columnar formation of grains [45]. As a result, LPBF-built samples have increased tensile strength and ductility. Using the SAAT condition, there was significant grain growth or rearrangement, as demonstrated by comparing the microstructures exhibited and also similar observation was seen in [46]. However, when the sample was dual aged at 490 °C after undergoing solution treatment at 940 °C, the previously complex microstructure that was formed by the LPBF process was eliminated, and finer martensite grains were generated, as seen in Fig. 8g–i. Here, the crystal of X and XR samples is randomly oriented, as shown in Fig. 8g, i, and it was supported by the pole figure of Fig. 8p, r, and XY samples are textured as shown
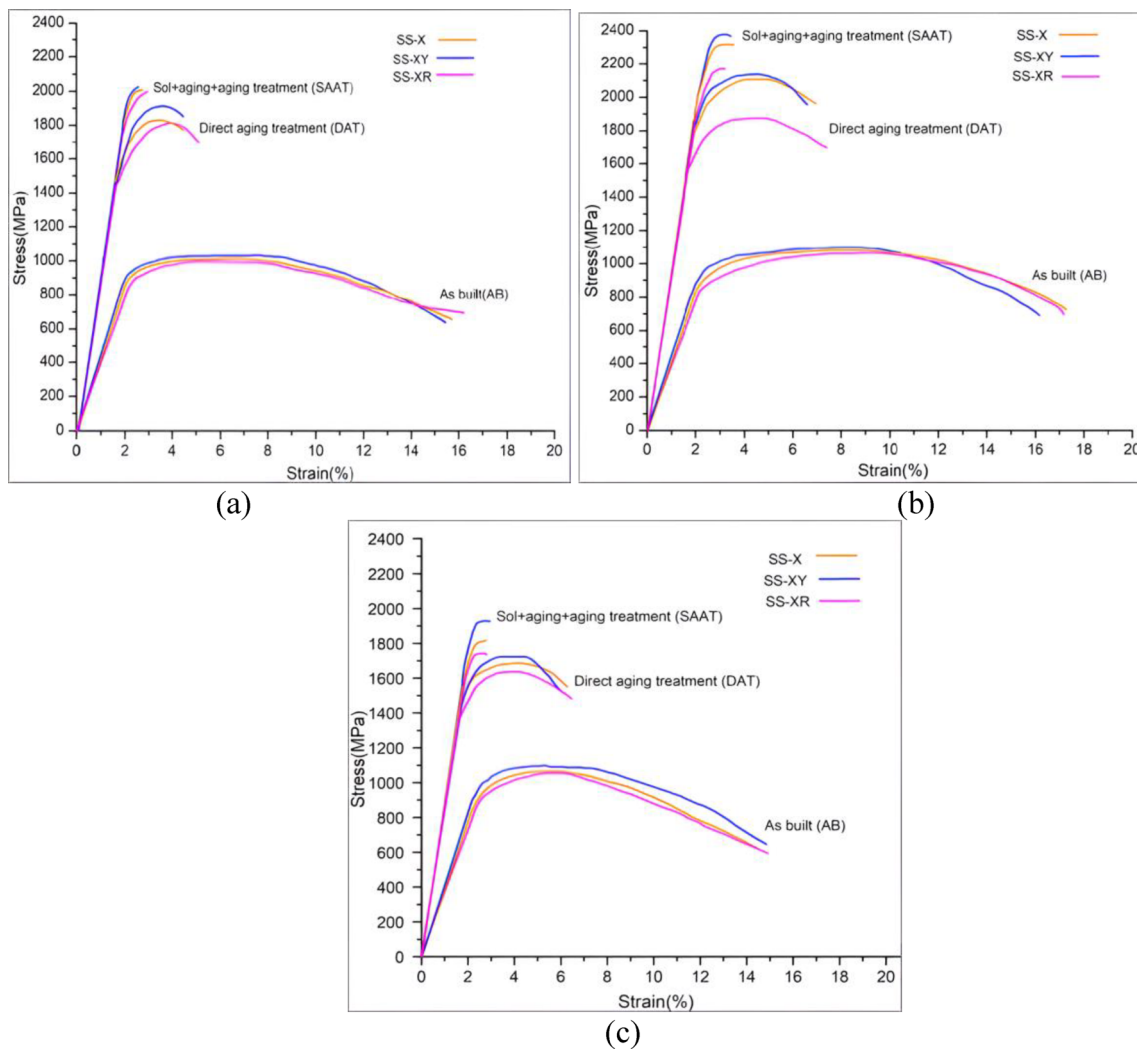

Fig. 9 Stress–strain curves characterization in relation to scanning techniques (SS-X, SS-XY, and SS-XR) at build orientation of **a** YX, **b** XZ, and **c** ZX

in Fig. 8h and displayed in the pole figure in Fig. 8q. This might imply that the phase was recrystallized during the SAAT at 940 °C. EBSD study indicates that the scanning method affects the continuity of grain development across subsequent layers and the growth of grains within the melted track. A similar observation was seen in [47]. The single crystalline texture is not found in three of these strategies. Furthermore, elongated cells do not form perpendicular to the scanning direction or in plane with it. Additional TEM investigations are required to investigate whether elongated cells develop in the plane, leading to the possible formation of mono-crystalline structures. The XY scan strategy generates anisotropy by preferentially growing along both axes, while the perpendicular scan strategy generates anisotropy due to both axes growing by heat treatments simultaneously. Using a cross-direction strategy reduces texture for both build and scan directions, as demonstrated by [30]. The literature has reported that the mechanical properties,

of LPBF maraging Steel parts can be enhanced by varying texture formation through the implementation of various laser scan strategies [30, 40, 42].

3.4 Tensile properties

Figure 9a–c depicts engineering tensile stress–strain curves as built and as well as heat treatment conditions of the samples when scanned in various orientations and scanning techniques. It can be noticed that the strength of all heat-treated samples was higher than as-built (AB) manufactured samples by Prakash et al. [36]. Heat treatment of aged samples resulted in an increase in strength values with no loss of ductility. The specimens in as-printed samples had high ductility and low strength in all tensile directions, and examined elongations at the break between 15.5 and 16.5% and yield strengths between 1000 and 1050 MPa. Heat-treated samples displayed considerable strength of up to 2.39 GPa
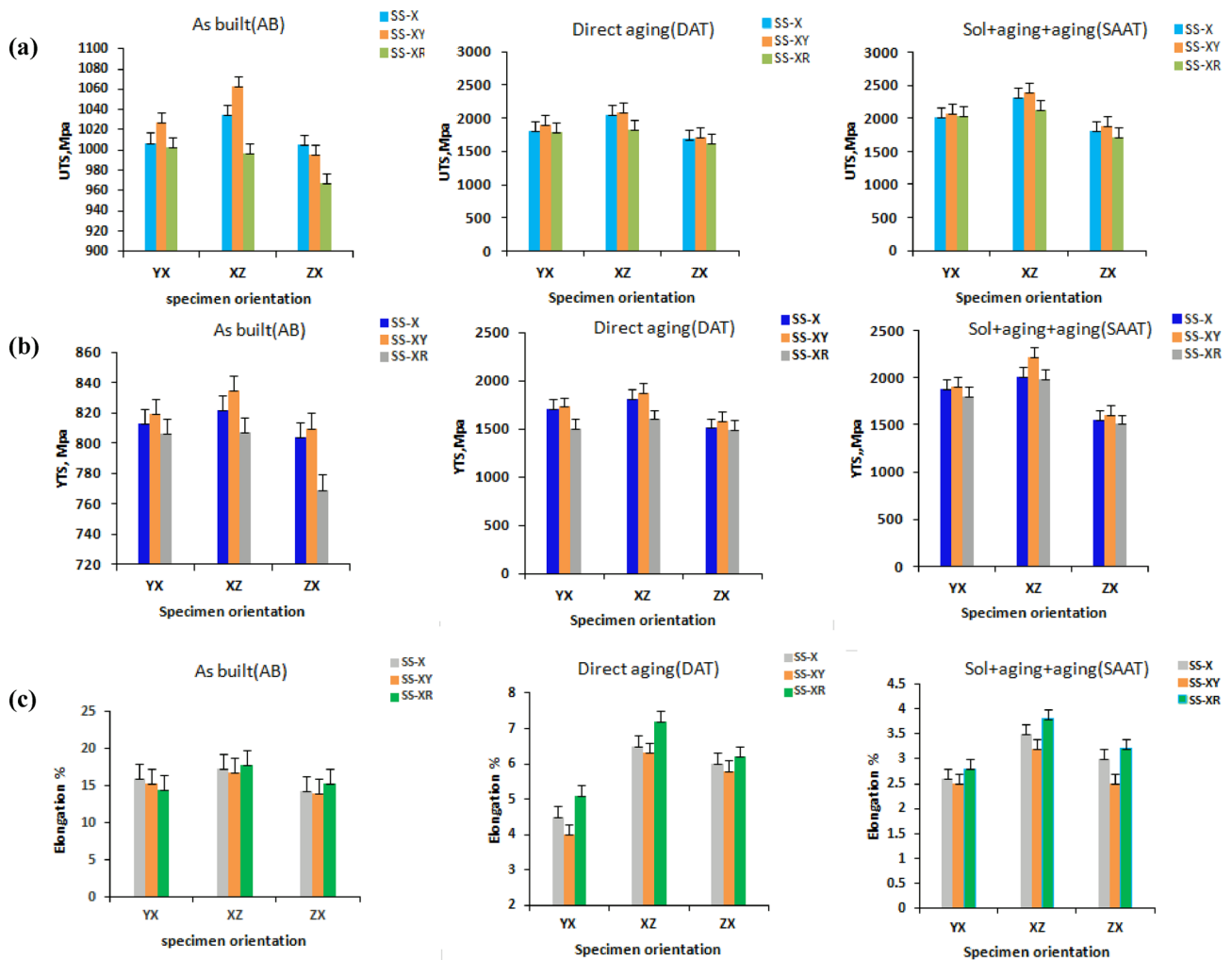
Fig. 10 Results of tensile testing of three orientations (YX, XZ, and ZX) with scan strategies (SS-X, SS-XY, and SS-XR) of the AB, DAT, and SAAT conditions for **a** UTS, **b** YS, and **c** % elongation

and modest extension of less than 3%, suggesting the development of fine nickel-rich intermetallic precipitates [13, 48]. Figure 9 shows that heat treatment affects stress–strain behavior differently depending on sample orientation. The maraging steel samples had the highest yield strength along the YX when aged at 490 °C without ST. When 490 °C dual aging was performed after 940 °C ST, the XZ orientation with XY scan strategy (SS-XY) was found to be the greater strength with ductility in both as-built and heat-treated conditions, as shown in Fig. 10. Similarly, UTS, YS, % elongation values have shown an improvement with following heat treatment.

In additive manufacturing's layer-by-layer processing, specimens produced in various orientations (YX, XZ, and ZX) with scan methods (X, XY, and XR) showed modest tensile anisotropy. The anisotropy was decreased due to the creation of an isotropic microstructure, the commencement of precipitation, and the release of residual stresses after heat treatment [15, 49]. The XZ-orientated AM sample exhibited the greatest ductility, owing to the most significant volume percentage of reversed austenite. Because of the coarse equiaxed grains in the HT samples, they had the lowest strength of all the tensile samples evaluated.

Using an aged specimen at 490 °C and solutionizing at 940 °C + aging followed by subsequent aging, the findings reveal a definite anisotropy of UTS, i.e., the sample's UTS was higher in the XZ direction than in the other two directions in the as-built state, the sample had almost isotropic tensile strength. When the samples were aged at 490 °C without the addition of ST, the yield and ultimate strength were significantly influenced by the tensile direction of the sample. In this instance, the YX and XZ samples demonstrated much more strength than the ZX sample. The high degree of crystallographic texture in the DAT and SAAT samples explains the substantial anisotropy in these samples.

The sample aged at 490 °C following 940 °C ST, followed by additional aging, revealed strong anisotropy, despite the heat treatment weakening the texture. YTS and UTS were lower in the ZX direction than in other directions. This means that the anisotropy of LPBF maraging steel is caused by more than just the crystallographic texture. It is also caused by the shape and size of the grains and how they are distributed. DAT samples showed less anisotropy than SAAT samples in Fig. 8d. As observed, heat treatment affected grain shape [46] in this case also. The significant mechanical anisotropy of LPBF-generated maraging steel is connected to its peculiar grain shape and high crystallographic texture. The strength of maraging steel is most affected by precipitation hardening, not cell structure. Both heat treatments produced equivalent tensile properties.

Figure 10 shows changes in microhardness and tensile strength between AB, DAT, and SAAT samples. Both the microhardness and the tensile strength of the material are found to be significantly lowered after solutionizing. Rapid cooling causes the molten pool to solidify into martensite tissue, small grains, and significant residual stress, all of which hinder dislocations' motion and fractures' growth. The microhardness and tensile strength are enhanced as a result. After being subjected to solutionizing and dual aging, microstructures transform into martensite lathes. Because of these modifications, martensite reduces some of its microhardness and tensile strength, as found in [16]. As grain refinement is achieved, residual stress and refined grains disappear after solutionizing, and their strengthening effects decrease simultaneously. Compared to residual stress disappearance and fine gain disappearance, the martensite transformation provides a less significant improvement. Microhardness and tensile strength eventually decrease. These results suggest that ductile fractures are predominant in both as-built and solutionized samples [50]. Fractures in transgranular regions are always ductile [51].

Because of the fast cooling and consolidation of build components that result in a superior morphology during the LPBF technique, the mechanical properties are much stronger than those obtained with traditional materials. The ultimate tensile strength measured in the XZ and YX measurements is significantly greater than the yield stress of 1000 MPa, indicating considerable plastic deformation. The variation in tensile strength between UTS and YTS of the samples generated in the ZX direction in the SAAT phase is 550 MPa, indicating that the studied cracks create minor plastic deformations. The heat-treated samples had greater tensile strength than the as-built. In addition, each sample
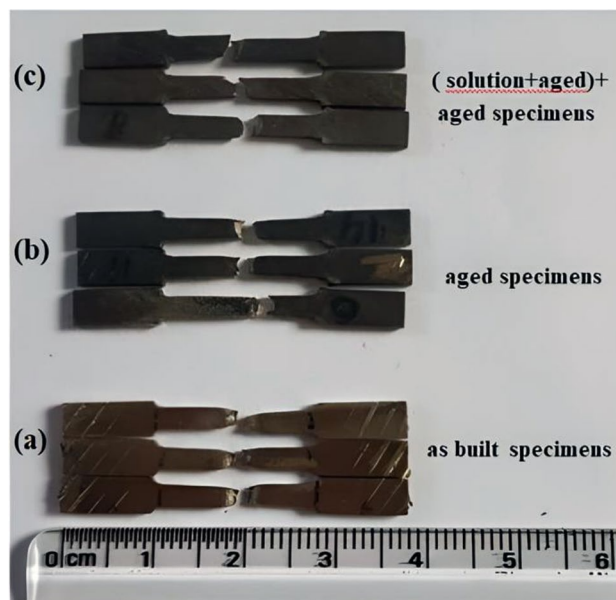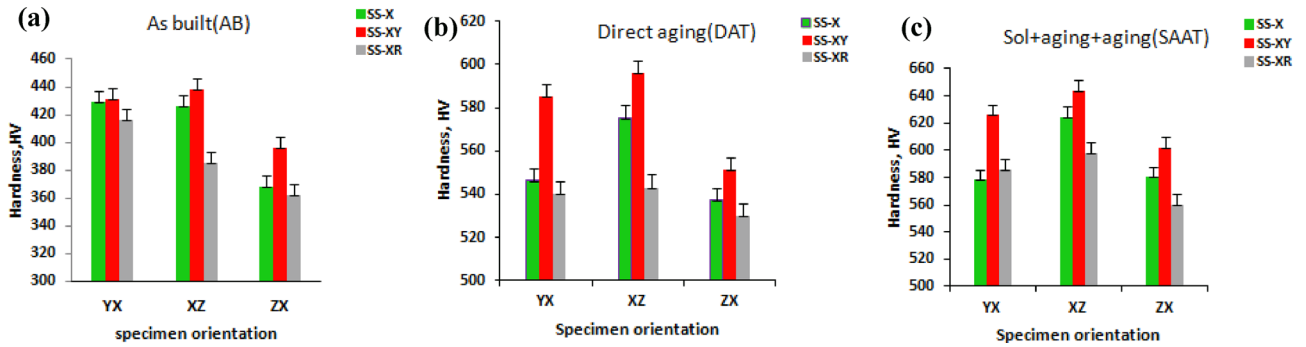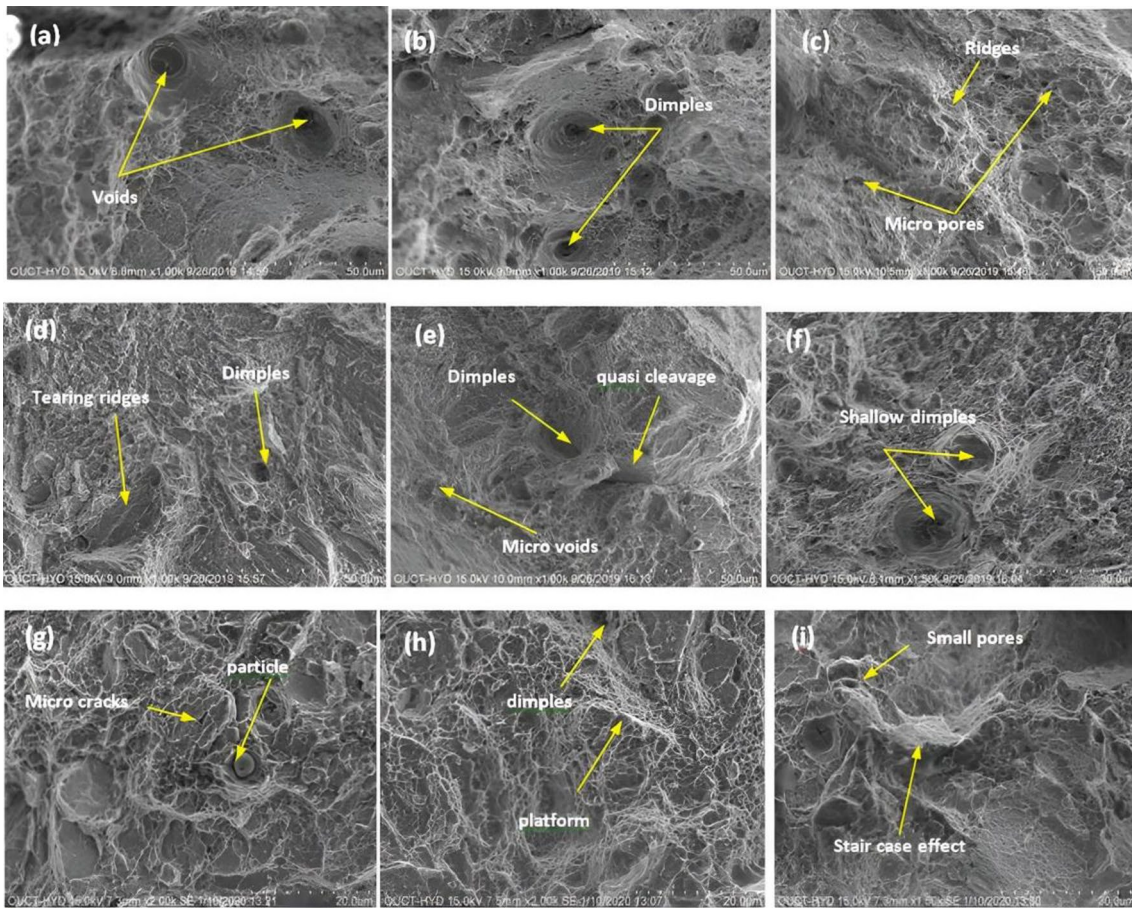

Fig. 11 Tensile specimens after the fracture

Fig. 12 Microhardness for **a** YX, **b** XZ, and **c** ZX build orientations at various scan strategies (SS-X, SS-XY, and SS-XR) under AB, DAT, and SAAT conditions

Fig. 13 Fracture morphology of sample as build by LPBF for **a** X, **b** XY, and **c** XR scan strategy. Direct aging treatment (DAT) for **d** X, **e** XY, and **f** XR scan strategy and solution + aging + aging treatment (SAAT) for **g** X, **h** XY, and **i** XR scan strategy

had ductile fracture morphologies, which were associated with the martensitic phase and were discovered in all of the building directions.

These samples have an ultimate tensile strength more significant than the yield strength of 1000 MPa, which indicates that plastic deformation produced a high strength. A low strength by plastic deformation resulting in certain fractures displayed in Fig. 13 is indicated by the difference of 550 MPa between the ultimate tensile strength and the yield strength of the samples formed in the ZX direction. The tensile test analysis revealed all specimen fractures occurred in the center of the grip, as shown in Fig. 11.

3.5 Microhardness

Figure 12 illustrates maraging steel hardness under various scan and post-heat treatment conditions. The hardness remained unchanged regardless of building directly under the as-built conditions around 430 Hv. Thus, the microhardness of the LPBF-produced maraging steel is unaffected by mechanical anisotropy. With the post-heat treatments, the hardness increased significantly. To explain this behavior, it is necessary to look at the strengthening mechanism, which has been demonstrated in numerous other studies [19, 48–50]. During aging, fine nickel-rich intermetallic precipitates are distributed evenly throughout the ductile low-carbon martensite structure. The maximum hardness of the sample after aging treatment was 435–545 Hv at XZ orientation when aging temperature was 490 °C for the scan strategy (SS-XY). Following post-heat treatments with solutionizing and aging, there was a noticeable difference in the hardness of the sample (SAAT). Scan approach (SS-XZ) at XZ orientation yielded the maximum hardness in the sample at 625 Hv. Hardness differences across samples with different post-heat conditions were only slightly noticeable in this case, with the sample that had been aged showing a lower hardness than the other samples by 80 Hv. Whereas the average test sample's hardness was around 600 Hv, the aging condition had almost little effect on scan techniques with various orientations.

Postprocessing is greatly affected by support structures and their dimensional tolerances in part fabrication. Further, powder morphology and characteristics play a significant role in microhardness [52]. The observed microhardness difference in the scanning and melt phases is attributed to a change in the volume of the α-martensite phase during the remixing of the prior layers during the scanning and melt phases. For an XY scan method, the repeated layer-by-layer deposition results in manufactured parts with varying physical and mechanical properties as a result of the variation in microhardness and orientation between layers. This is a challenge to completing the AM cycle. The hardness values for the YX orientation are found to be greater in the SAAT condition than in the DAT condition. With both post-treatment processes, the ZX orientation has lower hardness values due to its increased porosity and partially molten particles. After HT, the average micro Vickers hardness values improved from 435 to 545 HV, showing a 25% improvement over as-built. In grain boundaries, precipitation of γ phase stops grain growth and causes nucleation of strengthening phases' [46] results improving hardness. This study found that YX builds directions are associated with higher hardness values and better mechanical quality maraging steel may be made utilizing the LPBF technique.

3.6 Fractographic analysis

The fracture surface morphology of the as-built, DAT, and SAAT samples for the X, XY, and XR scanning techniques is shown in Fig. 13. In As-built state as suggested by K S Prakash et al. [37]. In X-scan approach Fig. 13a, perfect nucleation detects increased elongation, and unmelted zones and splats cause voids and cavities. XY scanning reveals enormous dimples in Fig. 13(b), causing plastic deformation. Also sample with micropores and ridges is also very rough due to weakly bound powder particles, as shown in Fig. 13c, which may be considered a porous structure.

Direct aging treatment (DAT) of X, XY, and XR scan strategies is shown in Fig. 13. For X Strategy, large areas of the fracture surface where dimples occur, as seen in Fig. 13d, lead to ductility. In addition, tearing patterns and micro-voids have been found. Crack propagation is slowed because of the greater energy absorption in the tear-tearing ridges. And for the XY strategy, there are obvious cleavage fractures, and the shallow dimples are observed in Fig. 13e and are limited. Thus, insufficient plastic deformation exists, and the cleavage fracture is a brittle fracture indicating that the development largely followed a quasi-cleavage mechanism [51]. Also, for the XR strategy, apparent shallow dimples are observed in Fig. 13(f). As a result, the elongation is high, which indicates high plasticity. Meanwhile, a deep hole formed by shrinkage of the molten liquid or vaporization directly corresponds to the LPBF process.

Also, for solution + aging + aging treatment (SAAT), conditions of X, XY, and XR scan strategies are shown in Fig. 13. As seen in Fig. 13g, microcracks were detected due to increased stress concentration. The residual stress was not completely relieved after heat treatment with a slow cooling rate. As a result, microcracks were easily formed due to stress concentration caused by second-phase particles. As seen in Fig. 13h, a tiny platform and dimples are found, indicating that the growth of cracks was mostly controlled by a quasi-cleavage mechanism [53, 54]. The fractures with a few pores are observed in Fig. 12i, which may cause stress concentration during the stretching process, thus reducing the plasticity of the material. When solution-aged-aged, the fracture surfaces had a staircase-like pattern. It exhibited cleavage fracture of the primary grain. Also, the solution-dual aging-treated specimen exhibited brittle fractures and small dimples. The fractures are brittle, with little plastic deformation for the DAT and SAAT samples. Therefore, the LPBF-produced maraging steels, treated with an integrated solution—dual aging is more advantageous than the aging process to obtain novel mechanical properties.

4 Conclusions

This work examined the effects of heat treatment experiments on the surface morphology, texture, phase transformation, and mechanical properties of MS1 material fabricated with LPBF under different heating conditions, i.e., direct aging treatment (DAT) and solution + aging + aging treatment (SAAT) under three scanning strategies and build orientation. A summary of the conclusions is given below.

- Heat treatments enhanced the hardness and tensile strength of LPBF-produced MS. In addition, it is hardness and tensile properties exhibited remarkable improvements in orientation-dependent anisotropy based on LPBF. Due to the dual-age treatment, mechanical anisotropy was eliminated by heat treatment.
- The findings of the tensile tests indicate that a different heat treatment condition may be necessary to get the maximum mechanical strength for the maraging steels generated by LPBF. In this way, the ductility of components is substantially improved by the built orientation. For edge-oriented components, SAAT results in higher tensile properties and fracture elongation. LPBF parts is recommended for better quality of MS parts using edge-oriented (XZ) with XY scan strategies. In SAAT is superior to direct aging treatment (DAT) for parts manufactured with complex shapes.
- The tensile test showed that the Z-oriented samples were the weakest in yield and ultimate tensile strength and that their brittle planar fracture features were perpendicular to the build orientation. In the vicinity of the substrate, the YX and XZ samples exhibited brittle failure characteristics, while the faraway regions showed ductile fracture characteristics.
- Heat treatment, including YS, UTS, and microhardness, significantly affects the mechanical properties of materials. The YS, UTS, and hardness of solutions treated at 940 °C for 2 h were reduced. In contrast, samples aged at 490 °C for 2 h exhibited peak values for YS, UTS, and microhardness. Moreover, due to their anisotropy, the horizontally built samples had slightly higher tensile behavior than the vertically built samples.
- The scanning electron micrographs of the fracture surfaces showed deficiencies, such as pores, dimples, and unmelted or partly melted powder particles. The results of the mechanical tests revealed that the defects had a noticeable effect. However, the findings of the tensile test and the hardness test were consistent with the previously reported data.
- In both yx and zx orientations, built samples revealed pores and cracks that influence strength and elongation.

- All samples showed brittle fracture morphologies associated with the martensitic phase in all building directions.
- XRD revealed austenite reversion and possible phase transformations
- Changes in microstructure influence the mechanical properties of various building orientations. In addition, samples made in the vertical direction perform lower than those made in the horizontal direction
- The texture remained strong in the solution + dual aging treatment (SAAT) and weak in the direct aging treatment (DAT)
- The scan direction is bi-directional along the build direction; a strong < 110 > texture and a weak < 100 > texture are found along the scan path. The 67° rotation of the scans caused a misalignment in the position of the melt pools in each layer, breaking the epitaxial growth of columnar formation and resulting fiber texture.
- This work is helpful for industrial guidance of an LPBF-produced maraging steel applications.

5 Future work

With the hot isostatic pressing (HIP) to produce fully dense components and eliminate porosity, casting defects and maraging steel manufactured by cold spray additive manufacturing is being improved in terms of its microstructure and mechanical anisotropy. The effect of the build orientation on the fatigue, tribological properties, and fracture modes of LPBF Maraging steel are to be investigated. Also, the machine learning algorithms are used in this LPBF process to enhance its quality and reliability.

Declarations

Conflict of interest The authors declare no conflict of interest.

References

1. Gu D, Shi X, Poprawe R, Bourell DL, Setchi R, Zhu J (2021) Material-structure-performance integrated laser-metal additive manufacturing. Science 372:6545
2. Chadha U, Abrol A, Vora NP, Tiwari A, Shanker SK, Selvaraj SK (2022) Performance evaluation of 3D printing technologies: a review, recent advances, current challenges, and future directions. Prog Addit Manuf 7(5):853–886
3. Feng Q, Tang Q, Liu Y, Setchi R, Soe S, Ma S, Bai L (2018) Quasi-static analysis of mechanical properties of Ti6Al4V lattice structures manufactured using selective laser melting. Int J Adv Manuf Technol 94:2301–2313
4. Liu Y, Xu H, Zhu L, Wang X, Han Q, Li S, Wang Y, Setchi R, Wang D (2021) Investigation into the microstructure and dynamic compressive properties of selective laser melted

Ti–6Al–4V alloy with different heating treatments. J Mater Sci Eng A 805:140561

5. Song J, Tang Q, Feng Q, Han Q, Ma S, Chen H, Guo F, Setchi R (2022) Effect of remelting processes on the microstructure and mechanical behaviours of 18Ni-300 maraging steel manufactured by selective laser melting. Mater Char 184:111648

6. Aboulkhair NT, Everitt NM, Ashcroft I, Tuck C (2014) Reducing porosity in AlSi10Mg parts processed by selective laser melting. Addit Manuf 1:77–86

7. Han Q, Gu Y, Setchi R, Lacan F, Johnston R, Evans SL, Yang S (2019) Additive manufacturing of high-strength crack-free Ni-based Hastelloy X superalloy. Addit Manuf 30:100919

8. Jagle EA, Choi PP, Van Humbeeck J, Raabe D (2014) Precipitation and austenite reversion behavior of a maraging steel produced by selective laser melting. J Mater Res 29:2072–2079

9. Chadha U, Selvaraj SK, Lamsal AS, Maddini Y, Ravinuthala AK, Choudhary B, Adefris A (2022) Directed energy deposition via artificial intelligence-enabled approaches. Complexity 2022:1–32

10. Dharnidharka M, Chadha U, Dasari LM, Paliwal A, Surya Y, Selvaraj SK (2021) Optical tomography in additive manufacturing: a review, processes, open problems, and new opportunities. Eur Phys J Plus 136(11):1133

11. Casalino G, Campanelli SL, Contuzzi N, Ludovico AD (2015) Experimental investigation and statistical optimisation of the selective laser melting process of a maraging steel. Opt Laser Technol 65:151–158

12. Croccolo D, de Agostinis M, Fini S, Olmi G, Vranic A, Ciric-Kostic S (2016) Influence of the build orientation on the fatigue strength of EOS maraging steel produced by additive metal machine. Fatig Fract Eng Mater Struct 39:637–647

13. Kempen K, Yasa E, Thijs L, Kruth JP, van Humbeeck J (2011) Microstructure and mechanical properties of selective laser melted 18Ni-300 steel. Phys Procedia 12:255–263

14. Tan, C, Zhou K, Tong X, Huang Y, Li J, Ma W, Kuang T (2017) Microstructure and Mechanical Properties of 18Ni-300 Maraging Steel Fabricated by Selective Laser Melting. In: Inter Conf on Adva Desi and Manuf Eng, South China University of Technology, Guangzhou, pp 404–410

15. Bai Y, Yang Y, Wang D, Zhang M (2017) Influence mechanism of parameters process and mechanical properties evolution mechanism of maraging steel 300 by selective laser melting. Mater Sci Eng A 703:116–123

16. Bai Y, Wang D, Yang Y, Wang H (2019) Effect of heat treatment on the microstructure and mechanical properties of maraging steel by selective laser melting. Mater Sci Eng 760:105–117

17. Song J, Tang Q, Feng Q, Ma S, Setchi R, Liu Y, Han Q, Fan X, Zhang M (2019) Effect of heat treatment on microstructure and mechanical behaviours of 18Ni-300 maraging steel manufactured by selective laser melting. Opt Laser Technol 120:105725

18. Mutua J, Nakata S, Onda T, Chen ZC (2018) Optimization of selective laser melting parameters and influence of post heat treatment on microstructure and mechanical properties of maraging steel. Mater Des 139:486–497

19. Tan C, Zhou K, Ma W, Zhang P, Liu M, Kuang T (2017) Microstructural evolution, nanoprecipitation behavior and mechanical properties of selective laser melted high-performance grade 300 maraging steel. Mater Des 134:23–34

20. Pardal JM, Tavares SSM, Terra VF, da Silva MR, dos Santos DR (2015) Modeling of precipitation hardening during the aging and over aging of 18Ni-Co-Mo-Ti maraging 300 steel. J Alloy Compd 393:109–111

21. Tewari R, Mazumder S, Batra IS, Dey GK, Banerjee S (2000) Precipitation in 18 wt. % maraging steel of grade 350. Acta Mater 48:1187–1200

22. Viswanathan UK, Dey GK, Sethumadhavan V (2005) Effects of austenite reversion during averaging on the mechanical properties of 18 Ni (350) maraging steel Mater. Sci Eng 398:367–372

23. Li X, Yin Z (1995) Reverted austenite during aging in 18Ni (350) maraging steel. Mater Lett 24:239–242

24. Paul MJ, Muniandy Y, Kruzic JJ, Ramamurty U, Gludovatz B (2022) Effect of heat treatment on the strength and fracture resistance of a laser powder bed fusion-processed 18Ni-300 maraging steel. Mater Sci Eng, A 844:143167

25. Oliveira AR, Diaz JAA, Nizes ADC, Jardini AL, Del Conte EG (2021) Investigation of building orientation and aging on strength–stiffness performance of additively manufactured maraging steel. J Mater Eng Perf 30:1479–1489

26. Vishwakarma J, Chattopadhyay K, Santhi Srinivas NC (2020) Effect of build orientation on microstructure and tensile behaviour of selective laser melted M300 maraging steel. Mater Scie and Eng A 798:140130

27. Meneghetti D, Rigon D, Cozzi W, Waldhauser MD (2017) Influence of build orientation on static and axial fatigue properties of maraging steel specimens produced by additive manufacturing. Procedia Struct Integr 7:149–157

28. Geiger F, Kunze K, Etter T (2016) Tailoring the texture of IN738LC processed by selective laser melting (SLM) by specific scanning strategies. Mat Sci Eng A 661:240–246

29. Gu D, Chen H (2018) Selective laser melting of high strength and toughness stainless steel parts: the roles of laser hatch style and part placement strategy. Mater Sci Eng A 725:419–427

30. AlMangour B, Grzesiak D, Yang JM (2017) Scanning strategies for texture and anisotropy tailoring during selective laser melting of TiC/316L stainless steel nanocomposites. J Alloys Compd 728:424–435

31. Condruz MR, Matache G, Paraschiv A, Frigioescu TF, Badea T (2020) Microstructural and tensile properties anisotropy of selective laser melting manufactured in 625. Materials 13(21):4829

32. Liu CY, Tong JD, Jiang MG, Chen ZW, Xu G, Liao HB, Lao CS (2019) Effect of scanning strategy on microstructure and mechanical properties of selective laser melted reduced activation ferritic/martensitic steel. Mater Sci Eng: A 766:138364

33. Suryawanshi J, Prashanth KG, Ramamurty U (2017) Tensile, fracture, and fatigue crack growth properties of a 3D printed maraging steel through selective laser melting. J Alloy Comp 725:355–364

34. Prevey PS (1986) X-ray diffraction residual stress techniques. ASM Int Handb 10:380–392

35. Karlapudy SP, Nancharaiah T, Rao VS (2023) Experimental optimization on mechanical properties of 18Ni-300 maraging steel produced by direct metal laser sintering. Eng Res Exp 5(1):015073

36. Karlapudy SP, Nancharaiah T, Rao VS (2021) Influence of different build orientation and laser scan strategies on surface quality, mechanical and material characteristics of 18 Ni-300 maraging steel processed through DMLS. Aust J Mech Eng 21:1–15

37. Casati R, Lemke JN, Tuissi A, Vedani M (2016) Aging behaviour and mechanical performance of 18-Ni 300 steel processed by selective laser melting. Metals 9:218

38. Pereloma EV, Shekhter A, Miller MK, Ringer SP (2004) Aging behaviour of an Fe–20Ni–1.8Mn–1.6Ti–0.59Al (wt%) maraging alloy: clustering, precipitation and hardening. Acta Mater 52:5589–5602

39. Bhardwaj T, Shukla M (2018) Effect of laser scanning strategies on texture, physical and mechanical properties of laser-sintered maraging steel. Mater Sci Eng: A 734:102–109

40. Thijs L, Kempen K, Kruth JP, Van Humbeeck J (2013) Fine-structured aluminium products with controllable texture by selective laser melting of pre-alloyed AlSi10Mg powder. Acta Mater 61:1809–1819

41. Marattukalam JJ, Karlsson D, Pacheco V, Beran P, Wiklund U, Jansson U, Hjörvarsson B, Sahlberg M (2020) The effect of laser scanning strategies on texture, mechanical properties, and site-specific grain orientation in selective laser melted 316L SS. Mater Des 193:108852

42. Ishimoto T, Hagihara K, Hisamoto K, Sun SH, Nakano T (2017) Crystallographic texture control of beta-type Ti–15Mo–5Zr–3Al alloy by selective laser melting for the development of novel implants with a biocompatible low Young's modulus. Scripta Mater 132:34–38

43. Podgornik B, Šinko M, Godec M (2021) Dependence of the wear resistance of additive-manufactured maraging steel on the build direction and heat treatment. Add Manuf 46:102123

44. Tan C, Zhou K, Kuang M, Ma W, Kuang T (2018) Microstructural characterization and properties of selective laser melted maraging steel with different build directions. Sci Tech Adv Mater 19(1):746–758

45. Sun Q, Guo K, Wang X, Liu J, Sun J (2020) Effect of scanning strategies on the microstructure and mechanical behavior of 316L stainless steel fabricated by selective laser melting. Mat Sci Engi: A 793:139879

46. Kim D, Kim T, Ha K, Oak JJ, Jeon JB, Park Y, Lee W.(2020). Effect of heat treatment condition on microstructural and mechanical anisotropies of selective laser melted maraging 18Ni-300 steel. Metals. 10(3):410.

47. Zhao C, Bai Y, Zhang Y, Wang X, Xue JM, Wang H (2021) Influence of scanning strategy and building direction on microstructure and corrosion behaviour of selective laser melted 316L stainless steel. Mater Des 209:109999

48. Kürnsteiner P, Wilms MB, Weisheit A, Barriobero-Vila P, Jägle EA, Raabe D (2017) Massive nanoprecipitation in a Fe-19Ni-xAl maraging steel triggered by the intrinsic heat treatment during laser metal deposition. Acta Mater 129:52–60

49. Yin S, Chen C, Yan X, Feng X, Jenkins R, O'Reilly P, Liu M, Li H, Lupoi R (2018) The influence of aging temperature and aging time on the mechanical and tribological properties of selective laser, melted maraging 18Ni-300 steel. Addit Manuf 22:592–600

50. Campanelli SL, Contuzzi N, Ludovico AD (2010) Manufacturing of 18 Ni Maraging 300 steel samples by selective laser melting. Adv Mat Res 83:850–857

51. Yasa E, Kempen K, Kruth JP (2010) Microstructure and mechanical properties of maraging steel 300 after selective laser melting. In: Proceedings of the Solid Freeform Fabrication Sympos Proceed, pp 383–396

52. Chadha U, Selvaraj SK, Abraham AS, Khanna M, Mishra A, Sachdeva I, Dhanalakshmi S (2023) Powder bed fusion via machine learning-enabled approaches. Complexity 2023:1–25

53. Kurz W, Fisher DJ (1998) Fundamentals of solidification, 3rd edn. Trans Tech Publ, p 316

54. Dewangan S, Selvaraj SK, Karthikeyan B, Chadha U, Singhal P, Sarma PP, Kumar MP (2022) Fractography analysis into low-C steel undergone through various destructive mechanical tests. Mater Res Exp 9(12):126502

55. EOS Maraging steel MS1 (2022) (http://eos.info.net/materials-data-sheets/eos-maraging-steel-ms1-msd.pdf)